Modeling of dynamic process in the laser-off period during laser drilling

Tingzhong Zhang (张廷忠)*, Xiaowu Ni (倪晓武), and Jian Lu (陆 健)**

School of Science, Nanjing University of Science and Technology, Nanjing 210094, China
**Corresponding author: zhangtingzhong0814@126.com; **corresponding author: lujian@njust.edu.cn*

Received April 5, 2015; accepted May 27, 2015; posted online July 3, 2015

A two-dimensional, transient model is proposed to study the dynamic process of keyhole formation and the material changes during both the laser-on and -off periods. The keyhole shape, temperature field, and velocity field are analyzed. The results indicate that the dynamic changes of the target material in the laser-off period have a great influence on the final structure of the keyhole.

OCIS codes: 000.4430, 140.3330, 140.3390, 160.3900.
doi: 10.3788/COL201513.081403.

Laser processing is of great importance in modern industry due to its advantages, which include low cost, fast speed, and high accuracy[1]. During laser manufacturing, the laser beam is focused on the work piece to create specific structures via its thermal effects[2]. It is worth noting that the laser-matter interaction involves complex physical processes, including heating, melting, evaporation, boiling, melt ejection, and plasma generation, etc.[3]. In order to analyze the laser manufacturing process, both experimental and numerical methods have been widely used[4–15]. Voisey *et al.*[4] discussed melt ejection during experimental laser drilling. Wei *et al.*[5] experimentally studied the mechanisms of spiking and humping formation in keyhole welding. However, it is difficult to observe the dynamic changes in the whole process using experimental methods, since they often have complex operating steps and expensive setups. Numerical simulations have overcome these drawbacks and can depict the complex phenomena with high accuracy and efficiency. The Level Set Method[9–11] and the volume of fluid method[12–14] are two approaches that are often used to simulate the dynamic process in laser manufacturing. With these methods, laser drilling, cutting, and welding can be well described. Zhang *et al.*[11] simulated the morphology of the keyhole with various laser pulse durations during laser drilling. Ganesh *et al.*[13] studied the processes of melting and solidification in the melt pool. Leitz *et al.*[14] presented the flow phenomena of the metal vapor inside the keyhole, and Song *et al.*[15] simulated the temperature field of the target in the laser drilling process using the birth-death element method via ANSYS.

These numerical calculations are capable of reflecting the dynamic process of the laser-material interaction with high accuracy and resolution. However, most of these studies only focus on the keyhole evolution when the laser is on, and subsequent changes when the laser is powered off are rarely reported. In our study of laser drilling with the volume of fluid method, it is found that the shape of the keyhole still changes after the laser is powered off. The changes cannot be ignored because they clearly increase the depth of the keyhole and have an important influence on the final configuration of the keyhole.

Here, to the best of our knowledge, we are the first to present a two-dimensional transient laser keyhole-drilling model that is able to show the thermal and flow fields together with the evaporation process in order to study the dynamic process of laser-off period in detail. The proposed model could easily capture the solid-liquid and liquid-gas interfaces as well as describe the process of keyhole evolution in real time. Moreover, the effectiveness of the model is confirmed by the experiments.

The scheme of the numerical model is explained in Fig. 1. The laser pulse is focused on the target surface, and there is air above the target. The laser pulse can be adjusted with different energies and pulse widths, etc., and different target materials could be studied using this model. Additionally, the following basic assumptions are necessary in this model:

(1) The initial temperature is $T_0 = 300$ K.
(2) The molten metal and gas in the computation region are assumed to Newtonian and incompressible; the fluid flow is laminar flow.
(3) The properties of the metal in both liquid and solid form are constant and not affected by the temperature.
(4) The Boussinesq approximation is considered.

To reflect the laser-material interaction exactly, the numerical model considers a series of important physical

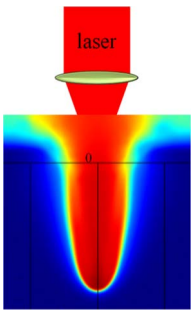

Fig. 1. Scheme of numerical model.

procedures such as phase change, heat and mass transfer, and fluid flow. The governing equations[16] are composed of conservation of mass, conservation of momentum, conservation of energy, and a volume fraction function[12], as

$$\frac{\partial \rho}{\partial t} + \mathrm{div}(\rho \mathbf{u}) = 0, \tag{1}$$

$$\frac{\partial \boldsymbol{u}}{\partial t} + \boldsymbol{u} \cdot \nabla \boldsymbol{u} = -\frac{1}{\rho}\nabla p + \nu \cdot \Delta \boldsymbol{u} + F_{sa} + F_{re} + \boldsymbol{g} - \frac{\boldsymbol{F}_{\mathrm{vol}}}{\rho}, \tag{2}$$

$$\frac{\partial E}{\partial t} + \boldsymbol{u} \cdot \nabla E = \frac{p}{\rho} + \mathrm{div}\,\boldsymbol{u} + \frac{k}{\rho}\Delta T + \frac{Q}{\rho}, \tag{3}$$

$$\frac{\partial \rho_i \phi_i}{\partial t} + \boldsymbol{u} \cdot \nabla \rho_i \phi_i = \rho_i \phi_i \mathrm{div}\,\boldsymbol{u}, \tag{4}$$

$$\rho = \sum_i \rho_i \phi_i, \rho E = \sum_i \rho_i E_i, k = \sum_i k_i \phi_i, \sum_i \phi_i = 1, \tag{5}$$

where E, F_{sa}, F_{re}, $\boldsymbol{g}$, $\boldsymbol{F}_{\mathrm{vol}}$, Q, p, $\boldsymbol{u}$, T, t, ϕ_i, k, ν, and ρ are the internal energy, surface tension, recoil pressure, gravitational acceleration, volume force, surface heat source, pressure, velocity, temperature, time, volume fraction function, thermal conductivity, kinematic viscosity, and density, respectively. The last term on the right-hand side in Eq. (2) represents the flow governed by Darcy's Law in the mushy zone[17]. When the mushy zone becomes completely solid at the liquid-solid interface, $\boldsymbol{F}_{\mathrm{vol}}$ goes to infinity and $\boldsymbol{u}$ is reduced to zero[18].

In Eq. (3), E is the internal energy and contains the enthalpy of melting and evaporation, which is described as a function of temperature according to[19]

$$E_s(T) = c_s(T) \qquad \text{(for solid metal)}, \tag{6a}$$

$$E_{\mathrm{mush}}(T) = E_s(T_m - dT) + L_m f_s \qquad \text{(for mushy region)}, \tag{6b}$$

$$E_l(T) = E_s(T_m - dT) + L_m + c_l(T - T_m - dT) \quad \text{(for liquid metal)}, \tag{6c}$$

$$E_v(T) = E_l(T_v) + L_v + (c_l + c_s)(T - T_v)/4 \quad \text{(for vapor metal)}, \tag{6d}$$

where f_s is the volume fraction of the solid metal in the mushy region[20], dT is the half-temperature interval across the mushy zone, c_s and c_l are the specific heat of the solid and liquid phase, $(c_l + c_s)/4$ is assumed to relate to the specific heat of the vapor, T_m and T_v are the melting and evaporation temperatures, and L_m and L_v are the latent heat of fusion and evaporation.

In Eq. (3), Q can be expressed as $Q = \eta I_q - q_{\mathrm{vap}}$. I_q is the laser power density, whose spatial distribution is Gaussian.

$$I_q = \frac{2E_0}{\pi r_0^2 \tau} \exp\left(-\frac{2x^2}{r_0^2}\right). \tag{7}$$

The temporal distribution of the laser is expressed as

$$g(t) = \begin{cases} 1, & 0 \le t \le \tau \\ 0, & t \ge \tau \end{cases}, \tag{8}$$

where E_0, τ, η, r_0 and x are the laser energy, pulse width, absorption coefficient of the material, focal radius, and the position, respectively. q_{vap} is the heat loss due to evaporation, which can be determined as $q_{\mathrm{vap}} = \rho v_{\mathrm{evp}} T_v$. Here, v_{evp} is free surface recession speed due to evaporation and is deduced by reading the work of Ki *et al.*[10].

To match up the above-mentioned governing equations, boundaries conditions are needed. On the exterior boundaries of the substrate, the heat efflux are calculated according to the local convection and thermal radiation, as given in

$$k\frac{\partial T}{\partial \boldsymbol{n}} = h_c(T - T_0) + \sigma_s \varepsilon (T^4 - T_0^4). \tag{9}$$

At the interface, the hydrodynamic boundary condition is also needed, and can be obtained as[21]

$$\mu \frac{\partial(\boldsymbol{u} \cdot \boldsymbol{s})}{\partial \boldsymbol{n}} = \frac{\partial \sigma}{\partial T}\frac{\partial T}{\partial \boldsymbol{s}}, \tag{10}$$

where $\frac{\partial \sigma}{\partial T}\frac{\partial T}{\partial \boldsymbol{s}}$ is the Marangoni effect. Such a driving force is caused by the gradient of the surface tension along the radial direction. $\boldsymbol{n}$ and $\boldsymbol{s}$ are the radial and tangential unit vectors of the free surface, respectively. σ_s is the Stefan–Boltzmann constant, ε is the surface emissivity, $\frac{\partial \sigma}{\partial T}$ is the temperature coefficient of the surface tension, h_c is the convective heat transfer coefficient, and T_0 is the ambient temperature.

The corresponding properties of the aluminum and constants used in the simulation are listed in Table 1.

In order to apply the numerical model, as well as verify its accuracy, corresponding experiments were implemented and the experimental data were compared with the simulation results, as discussed below.

Experiments were performed using a millisecond-pulsed Nd:YAG laser beam system (Melar-50) with a pulse width of 1000 μs, a wavelength of 1064 nm, and tunable energy. A flat aluminum sheet with a thickness of 4 mm was chosen as the target, and the laser beam was focused onto the front surface of the target with a focal radius of ~300 μm. The cross section of the keyhole was obtained via the wire cut method, and the diameter and depth of the drilled holes were measured using a reading microscope (JL107J). The features of the hole were also observed under this microscope. Figure 2(a) is the numerical result of the cross-sectional shape of the keyhole with irradiated laser energy of 4.86 J, while Fig. 2(b) shows the experimental result with the same conditions in the simulation. Comparisons of the keyhole shape for both the

Table 1. Properties of Aluminum and Constants in Simulation.[22,23]

Nomenclature (unit)	Symbol	Value
Melting/evaporation temperature (K)	T_m/T_v	933/793
Solid/liquid density (kg/m^3)	ρ_s/ρ_l	2702/2385
Solid/liquid specific heat (J/m/K)	c_s/c_l	917/1080
Solid/liquid conductivity (W/m/K)	k_s/k_l	237/100
Latent heat of fusion/ evaporation (J/kg)	L_m/L_v	3.6×10^5/ 1.09×10^7
Temperature coefficient of surface tension (N/m/K)	$\frac{\partial\sigma}{\partial T}$	-0.3×10^{-3}
Dynamic viscosity (Pa s)	μ	1.6×10^{-3}
Convective heat transfer coefficient (W/m^2/K)	h_c	20
Radiation emissivity (W/m^2/K^4)	ε	0.2
Absorption coefficient	η	0.26
Stefan–Boltzmann constant (W/m^2/K^4)	σ_s	5.67×10^8
Focal radius (μm)/Pulse width (μs)	r_0/τ	300/1000

simulation and the experiment indicate that the proposed numerical model accurately reflects the laser drilling process.

Moreover, in order to compare the numerical and experimental approaches quantitatively, the keyhole depth and width with different laser energies are also analyzed, as shown in Table. 2. With the higher laser energy, both the keyhole depth and width increase. Moreover, the numerical results fit well with the experimental data, which further proves the reliability of the numerical model.

With the certification of the numerical model, the laser drilling process in the experiment can be analyzed via numerical simulation for the sake of simplicity, high accuracy, and efficiency. Figure 3 illustrates the dynamic

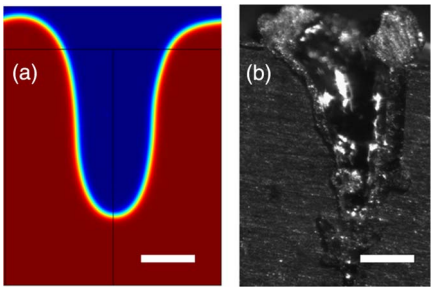

Fig. 2. (a) Numerical and (b) experimental comparisons of the keyhole shape with a laser energy of 4.86 J. The white bar represents 0.5 mm.

Table 2. Numerical and Experimental Data for Both Keyhole Depth and Width.

Energy (J)	Depth[a] (mm)	Depth[b] (mm)	Diameter[a] (mm)	Diameter[b] (mm)
1.22	0.894	0.902	0.518	0.523
2.07	1.322	1.313	0.752	0.741
3.13	1.448	1.420	0.824	0.817
4.86	1.523	1.510	0.872	0.870
6.31	2.070	2.109	0.863	0.875
8.01	2.745	2.693	0.901	0.920
10.20	3.120	3.131	0.943	0.958
13.27	3.439	3.357	1.052	1.046

[a]Experiment.
[b]Simulation.

process of the keyhole evolution at different moments in both the laser-on and laser-off periods with a laser energy of 4.86 J and a pulse width of 1000 μs. It is clear that in the laser-on period, the depth of the keyhole keeps increasing. However, when the laser pulse is off, the depth of the keyhole still increases. In fact, the keyhole depth increased by nearly 20% after the laser pulse was turned off. This reveals that studying the dynamic changes in the laser-off period is of great importance in laser manufacturing.

In order to analyze the dynamic processes in the laser-off period in detail, we also calculated the temperature fields, as shown in Fig. 4, with the same observation moments as Fig. 3. With the laser on, the temperature rapidly increased to reach the boiling temperature of aluminum (2793 K). Melting and evaporation occur almost simultaneously, and the vapor-induced recoil pressure squeezes the molten material out of the keyhole and ejects it into the air. Additionally, high temperature gradients on the melt pool surface lead to large surface tension gradients and induce the Maragoni convection: the thermo-capillary force drags the liquid metal from the irradiation center to

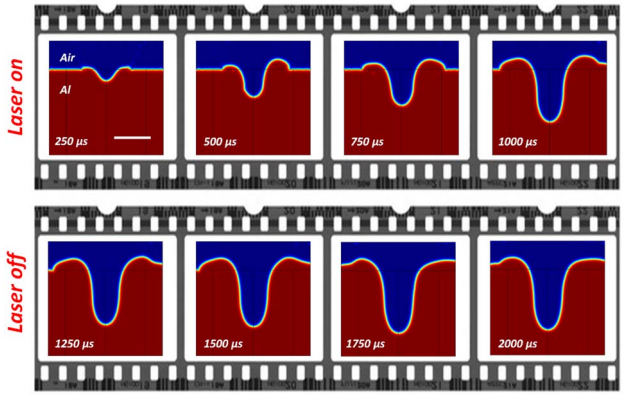

Fig. 3. Image sequences of the keyhole fabricated by a single laser pulse with a laser energy of 4.86 J in both the laser-on and -off periods. The white bar represents 1 mm.

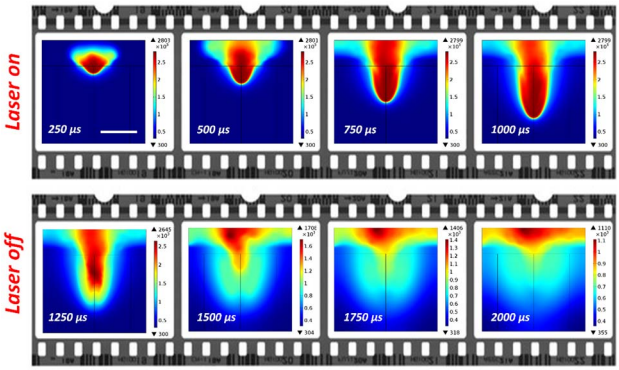

Fig. 4. Temperature distributions of the keyhole fabricated by a single laser pulse with a laser energy of 4.86 J in both the laser-on and -off periods. The white bar represents 1 mm.

the periphery of the melt pool and enhances the heat transfer in the lateral direction. With the laser off, the temperature decreases. But in the early stage of the laser-off period, the temperature remains higher than the melting temperature of aluminum (923 K), which still can induce material splash. However, in the late stage, as the temperature falls below aluminum's melting temperature, the liquid metal solidifies and accumulates in the bottom of the keyhole. So there is a tiny decrease in the keyhole depth later in the laser-off period.

The velocity of the splash shown in Fig. 5 is able to explain the dynamic process in both the laser-on and -off periods. As the temperature distribution goes higher than aluminum's boiling temperature, the splash is acute and obvious. In the laser-off period, as the temperature goes down, the splash rapidly decreases as well, since there is no more input energy. When the temperature is below aluminum's melting temperature, the splash nearly disappears.

The dynamic changes of the keyhole shape, temperature, and velocity fields shown in Figs. (3)–(5) depict the laser drilling process in both the laser-on and -off periods. From the simulation, we can conclude that not only is the process when the laser is on worth studying, since it has a great influence on the keyhole structure, but the dynamic process in laser-off stage is also of great importance. It is seen that the features of the keyhole still change when the laser is off.

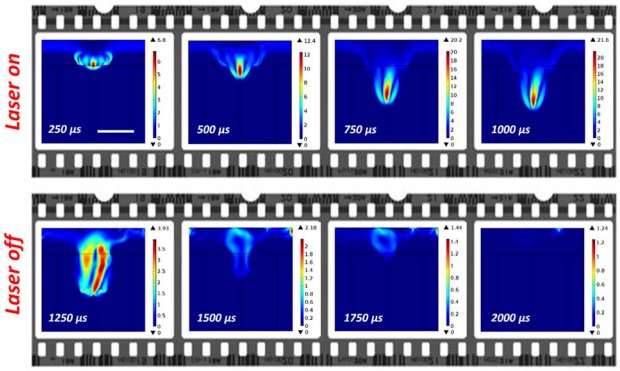

Fig. 5. Velocity distributions of the keyhole fabricated by a single laser pulse with a laser energy of 4.86 J in both the laser-on and -off periods. The white bar represents 1 mm.

In conclusion, a two-dimensional transient model for simulating millisecond-pulse laser drilling is proposed as an example to study the dynamic process in the laser-off period. With the quantitative analysis of the keyhole structure, temperature distribution, and velocity field, we clearly show that the dynamic changes in the laser-off period are of great significance in product quality control. The research proposes a potential way for detailed study and analysis during the laser-off period in laser manufacturing. Meanwhile, the study also provides guidance and a reference for double- and multi-pulse studies in laser manufacturing, in order to gain a better understanding of the energy coupling between the target and subsequent laser pulse.

This work was supported by the Program for Postgraduates Research Innovation at the University of Jiangsu Province under Grant No. KYLX_0341.

References

1. C. Xu, L. Jiang, N. Leng, Y. Yuan, P. Liu, C. Wang, and Y. Lu, Chin. Opt. Lett. **11**, 041403 (2013).
2. V. A. Serebryakov, M. V. Volkov, and X. Zhang, J. Opt. Technol. **72**, 241 (2005).
3. B. S. Yilbas and M. Sami, J. Phys. D: Appl. Phys **30**, 1996 (1997).
4. K. T. Voisey, S. S. Kudesia, W. S. O. Rodden, and T. W. Clyne, Mater. Sci. Eng. A **356**, 414 (2003).
5. P. S. Wei, K. C. Chuang, J. S. Ku, and T. DebRoy, IEEE Trans. Comp. Pack. Manuf. Technol. **2**, 383 (2012).
6. X. Yin and Y. Zhuang, Chin. Opt. Lett. **12**, 21409 (2014).
7. S. Juodkazis, K. Nishimura, and H. Misawa, Chin. Opt. Lett. **5**, S198 (2007).
8. F. Ji, L. Xu, and F. Li, Chin. Opt. Lett. **6**, 16 (2008).
9. J. A. Sethian and P. Smereka, Annu. Rev. Fluid Mech. **35**, 341 (2003).
10. H. Ki, P. S. Mohanty, and J. Mazumder, Metall. Mater. Trans. A **33**, 1817 (2002).
11. Y. Zhang, Z. Shen, and X. Ni, Int. J. Heat Mass Tran. **73**, 429 (2014).
12. C. W. Hirt and B. D. Nichols, J. Comput. Phys. **39**, 201 (1981).
13. R. K. Ganesh and A. Faghri, Int. J. Heat Mass Transfer **40**, 3351 (1997).
14. K. H. Leitz, H. Koch, and A. Otto, Appl. Phys. A-Mater **106**, 885 (2012).
15. L. S. Song, G. Q. Shi, and G. L. Zhan, Acta Armamentarii **27**, 879 (2006).
16. S. Fujii, N. Takahashi, S. Sakai, T. Nakabayashi, and M. Muro, Proc. SPIE **3888**, 218 (2000).
17. W. D. Bennon and F. P. Incropera, Int. J. Heat Mass Transfer **30**, 2161 (1987).
18. V. R. Voller and C. Prakash, Int. J. Heat Mass Transfer **30**, 1709 (1987).
19. W. D. Tan and Y. C. Shin, J. Phys. D: Appl. Phys. **47**, 345501 (2014).
20. J. W. Liu, Z. H. Rao, S. M. Liao, and P. C. Wang, Int. J. Adv. Manuf. Technol. **73**, 1705 (2014).
21. J. Zhou, H. L. Tsai, and T. F. Lehnhoff, J. Phys. D: Appl. Phys. **39**, 5338 (2006).
22. A. T. Dinsdale and P. N. Quested, J. Mater. Sci. **39**, 7221 (2004).
23. W. M. Rohsenow, J. P. Hartnett, and Y. I. Cho, *Hand book of Heat Transfer*, Vol. **3** (McGraw-Hill, 1998).